

Impact of resonant magnetic perturbations on zonal flows and microturbulence

Z.R. Williams^{1,2}, M.J. Pueschel³, P.W. Terry², T. Nishizawa² , D.M. Kriete⁴,
M.D. Nornberg² , J.S. Sarff², G.R. McKee⁴, D.M. Orlov⁵  and S.H. Nogami⁶ 

¹ Department of Physics, Hope College, Holland, Michigan 49423, United States of America

² Department of Physics, University of Wisconsin-Madison, Madison, Wisconsin 53706, United States of America

³ Institute for Fusion Studies, University of Texas at Austin, Austin, Texas 78712, United States of America

⁴ Department of Engineering Physics, University of Wisconsin-Madison, Madison, Wisconsin 53706, United States of America

⁵ University of California San Diego, La Jolla, CA 92093, United States of America

⁶ West Virginia University, Morgantown, WV 26506, United States of America

Received 30 April 2020, revised 1 June 2020

Accepted for publication 11 June 2020

Published 28 July 2020



CrossMark

Abstract

Results from a joint experimental and computational effort studying the effect of resonant magnetic perturbations (RMPs) on microturbulence levels and their connection to zonal flows in the DIII-D tokamak L-mode are presented. Beam emission spectroscopy measurements show a direct increase in density fluctuations at microturbulent scales with increasing RMP amplitude, suggesting that magnetic activity introduced by the RMP affects the regulation of microturbulence on DIII-D. This is analogous to how MHD-scale magnetic fluctuations arising from tearing modes have been observed in simulations to increase microturbulence levels in the reversed-field pinch (RFP). In the RFP, this is attributed to magnetic fluctuations eroding turbulence-limiting zonal flows; this work examines if a similar mechanism is present for DIII-D microturbulence. Gyrokinetic simulations find that the application of an RMP corresponds directly to a decrease in zonal flow levels, producing a similar increase of turbulent fluctuation levels over a range of RMP amplitudes as observed in the experiment.

Keywords: turbulence, transport, zonal flows, resonant magnetic perturbations, microturbulence, tokamak

(Some figures may appear in colour only in the online journal)

1. Introduction

A number of computational studies of plasma turbulence and transport have demonstrated the importance of including effects that couple disparate scales to accurately reproduce experimentally observed fluxes [1–3]. While these works use the term *multi-scale* to refer specifically to interactions between physics at ion and electron scales, there exists another set of cross-scale interactions important in determining transport values between large, MHD-like scales and ion scales. There exists already a significant body of theoretical literature

studying the interaction of large-scale magnetic structures (e.g. islands) and microturbulence in tokamaks [4–9]. However, the role that self-consistent zonal flows play in this interaction, specifically how magnetic fluctuations may erode zonal flows and subsequently increase microturbulence, has not been extensively explored.

As a specific example of a multi-scale interaction of large-scale magnetic fluctuations, zonal flows, and ion-scale microturbulence, observations on the Madison Symmetric Torus (MST) reversed-field pinch (RFP) show the coexistence of tearing modes at low frequencies and drift waves at higher

frequencies [10]. These large-scale tearing modes play an essential role in determining the saturation level of microturbulence in the improved-confinement operation regimes on MST [11, 12] through their degrading effect on zonal flows. Tearing modes produce radial magnetic fluctuations, which can result in a decrease of zonal flow amplitude [13–15]. The analytic calculation performed in reference [13] demonstrates that the introduction of a stochastic field perturbation results directly in the reduction of the Rosenbluth-Hinton residual, which is a well-known measure of characteristic zonal flow strength [16]. This zonal-flow erosion is driven by the fast movement of electrons along radially perturbed magnetic field lines. These electrons move off flux surfaces by following field lines with a perturbed component normal to the flux surface; if the perturbation is resonant in ballooning angle, or if field lines decorrelate (see reference [14]), they do not return to their original radial location. This scenario is found for a microstochastic magnetic field, in which the equilibrium field is entirely intact but the $\mathcal{O}(\rho^*)$ magnetic field lines have nonzero diffusivity. This decorrelation could occur due to other mechanisms such as collisions or electrostatic turbulence; however, this work will focus only on magnetic stochasticity as the decorrelation mechanism. When electrons are lost from their original flux surface, the resultant effect is a reduced electrostatic potential difference across flux surfaces, leading to a degraded zonal flow. For certain flavors of microinstability-driven turbulence, this reduction of zonal flow can lead to a subsequent increase in fluctuations and transport. This mechanism couples the dynamics between large tearing mode scales and small microturbulent scales and is a key focus of this work.

The reduction of zonal flow through magnetic fluctuations has been observed in gyrokinetic simulations of RFP plasmas [11, 12], in which computations that do not include tearing mode fluctuations vastly under-predict turbulence and transport levels. When including tearing mode fluctuations (modeled in references [11] and [12] as a fixed external perturbation on top of the self-consistent electromagnetic response of the plasma), the transport increases to levels that agree much more closely with experimental expectations. The present work seeks to explore whether this interaction among zonal flows, magnetic fluctuations, and microturbulence can occur in different fusion device contexts, using observations both from experimental measurements and theoretical predictions. In order to measure in a controlled way how turbulence and zonal flows vary with large-scale magnetic activity, it is desirable to have direct control over the amplitude of the large-scale magnetic fluctuations in question. In tokamaks, this is commonly done by introducing resonant magnetic perturbations (RMPs).

RMPs are large-scale magnetic fluctuations imposed on plasma equilibria through the use of currents driven in external coils. Importantly, they are used on tokamaks as a means of mitigating edge-localized modes (ELMs) [17], which otherwise result in large bursts of energy that can damage device components. While this presents a significant benefit in the efforts towards sustained confinement in tokamaks, there are still aspects of how RMPs affect plasma dynamics that are not fully understood. It has been noted that when using RMPs to

remove ELMs, high-frequency fluctuations arise [18]. As will be explored in this work, RMPs can play a significant role in governing turbulence and transport at small scales.

The concurrent presence of RMPs and microturbulence in tokamaks closely mirrors the tearing fluctuations and microturbulence found in the RFP, and provides an additional avenue for exploring interactions among zonal flows, microturbulence, and large-scale magnetic activity. Note that for three-dimensional magnetic geometries (like in the stellarator), zonal flows behave in a qualitatively different behavior than for axisymmetric devices. In such configurations, collisionless zonal flow decay attributed to phase mixing is observed (see reference [19]); this is a physically distinct process from the magnetic-fluctuation-induced zonal flow erosion described above, and is not examined in this work. For the purpose of investigating the physics of magnetic-flutter-induced zonal flow erosion via experimental means, tokamak RMPs have the distinct advantage over tearing modes in RFPs in that the amplitude can be set by user input to a desired level. Thus, measurements can be performed that map specific magnetic fluctuation amplitudes to corresponding microturbulence levels.

Experimental measurements described herein show variation of microturbulent density fluctuations with RMP amplitude, with increasing RMP amplitude corresponding to larger density fluctuations at microturbulence scales, consistent with the physical picture described above. These experimental discharges are studied in depth computationally. An increase in microturbulence activity due to an applied external magnetic perturbation is observed, both in wavenumber spectra of density fluctuations and in transport quantities. It is seen that flux-surface-breaking perturbations are necessary to achieve this observed physical effect, in contrast to previous work, which discussed flux-surface preserving (non-resonant in ballooning angle) perturbations and their lack of influence on transport levels [20].

This paper is organized as follows: in section 2, the experimental setup and measurements of variation of microturbulence with RMP amplitude are described, and a linear gyrokinetic characterization of the fluctuations is performed. Section 3 details computational studies of the effect on the RMP on microturbulence, how this effect connects to zonal flow dynamics, and the roles different specific properties of the RMP play. The results are then summarized in section 4.

2. Microturbulence in DIII-D L-Mode plasmas

A run campaign on the DIII-D tokamak has characterized the effect of RMPs on high-frequency, long-wavelength ($k_{\perp} \rho_s \lesssim 0.5$) density fluctuations measured using the beam emission spectroscopy (BES) diagnostic [21]. These studies used the internal I-coils [22] to generate the RMP field, varying the coil current in incremental steps over the course of an inner-wall-limited L-mode discharge of deuterium plasma. Density fluctuation spectra were measured with BES, which in this experiment was configured with an 8×8 array of channels. Scans in amplitude determined how both RMP magnitude and parity

affect microturbulence levels for $n = 1$ and $n = 3$ RMPs. Note that in this context, parity refers to even or odd with respect to the I-coil configuration and does not translate into even or odd parity of fluctuation structures in ballooning angle with respect to the outboard midplane; the latter is a common characterization of fluctuation structure and will be discussed later. In the gyrokinetic simulation results presented in section 3, resolving the largest spatial scales of $n = 1$ concurrently with microturbulence adds additional expense, and the assumption that parallel wavenumbers $k_{\parallel} \ll k_{\perp}$ are much smaller than their perpendicular counterparts utilized in the simulations breaks down at this scale. As such, this work focuses only on results from the RMP amplitude scan for the $n = 3$ perturbation. Additionally, the odd-parity RMP produced a more readily observable change in the turbulence spectra, so the discussion that follows concerns only $n = 3$, odd-parity RMP discharges (DIII-D discharges #172145 and #172146).

In these experiments, the current of the RMP I-coils is turned on, creating a small amplitude RMP (relative to ELM-suppression RMPs [17]) of $B_r/B_0 \approx 7.6 \times 10^{-5}$ and incrementally lowered, establishing four distinct phases of the discharge (see figure 1). Figure 2 shows profiles of electron density and temperature over different stages in the scan. It is evident from the figure that the RMP does not produce large changes to the radial profiles. This ramp-down scan in RMP amplitude is performed with the BES array centered at two different radial positions, measuring fluctuations spanning a total radial extent from $\psi = 0.67 - 1$, where ψ is the normalized poloidal flux coordinate, with $\psi = 1$ corresponding to the location of the unperturbed equilibrium flux surface touching the inner wall. Figure 3 shows BES measurements of the time-averaged wavenumber spectra of density fluctuations at $\psi = 0.88$ (corresponding to the $q = 10/3$ rational surface, see figure 4) for each phase of the RMP ramp-down. As the I-coil current is decreased, a corresponding decrease is observed in the density fluctuation levels in the $k_{\theta}\rho_s = 0.15 - 0.3$ range ($k_{\theta}\rho_s$ being normalized poloidal wavenumber), where ion-scale microturbulence tends to be active. These measurements are suggestive of the multi-scale physics on RFPs where MHD fluctuations lead to zonal-flow reduction, which consequently affects microturbulence levels [11, 12]. Previous efforts have measured properties of zonal flows in DIII-D [23, 24], but an experimental analysis of zonal flow amplitude for these discharges is beyond the scope of the present work.

To more thoroughly understand the experimentally observed effects, these discharges are studied using the gyrokinetic turbulence code GENE [26, 27]. Linear simulations elucidate the extent to which variations of the RMP amplitude affects equilibrium stability properties. Analysis was performed separately for each phase of the ramp-down scan at the radial location of interest ($\psi = 0.88$, corresponding to the $q = 10/3$ island), with input parameters generated from kinetic reconstructions [28–31] averaging over the time periods of the four different I-coil current steps, respectively. The magnetic geometry was determined separately for each stage in the RMP amplitude ramp down via TRACER-EFIT [32], which contains information about the equilibrium magnetic field configuration excluding RMP effects. Typical resolutions

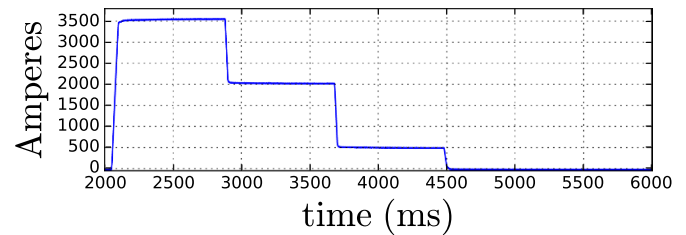


Figure 1. I-coil current as a function of time. The discharge is characterized by four distinct stages of RMP amplitude, with equilibrium quantities determined separately from time averages over each stage. For this work, the IU30 coil current is positive, and IL30 coil current is negative.

used for the linear calculations included 31 k_x (radial) modes, 16 z , 32 v_{\parallel} (parallel velocity), and 8 μ grid points, where z is the coordinate along the field line and μ is the magnetic moment. Relevant physical input parameters at each point of the RMP amplitude scan are given in table 1.

It is important to note that the simulations presented throughout this work use an artificially lowered value for the normalized electron pressure of $\beta = 10^{-4}$, approximately a factor of four lower than the average experimental β at this radial location. At the nominal β , a linear instability appears at low wavenumbers and persists for $k_y\rho_s < 0.005$, which corresponds to spatial scales exceeding the device size. Here, k_y is the binormal wavenumber as used in GENE (comparable to the experimental poloidal wavenumber), and ρ_s denotes the ion sound gyroradius. This mode drives high levels of electromagnetic turbulence in non-linear flux-tube simulations that never saturate. It is likely attributable to the inaccuracies of the flux-tube prescription that arise at very low k_y and therefore is deemed an artifact. When lowering β , this mode is not unstable. Note that ion-scale linear instabilities are not noticeably affected by the reduced β , so it is expected that using the lower value will not impact the microturbulent behavior. Additionally, altering β (and thus the self-consistent plasma electromagnetic response) will not qualitatively change the physics in question. As discussed, the mechanism by which magnetic fluctuations degrade zonal flow concerns the decorrelation of streaming particle trajectories from their original field lines. In principle, this can be achieved even in an entirely electrostatic ($\beta = 0$) plasma, provided there is some way of introducing stochasticity to the field. Maintaining a small but finite β , while not necessary to capture the physics of interest to the work, helps to reduce computational cost through the CFL condition

At $n = 1$, the simulations do not capture important physical effects, such as parallel derivatives in Ampère's Law, or boundary effects impacting MHD modes. Moderate quantitative corrections may be expected to result from these effects at $n = 3$, but will be ignored for the present simulations and analyses.

When analyzing the linear stability spectrum, shown in figure 5, one finds that across all of the RMP amplitudes, there exist a ∇T -driven trapped-electron mode (TEM, dashed lines) and an ion-temperature-gradient (ITG, solid lines) mode

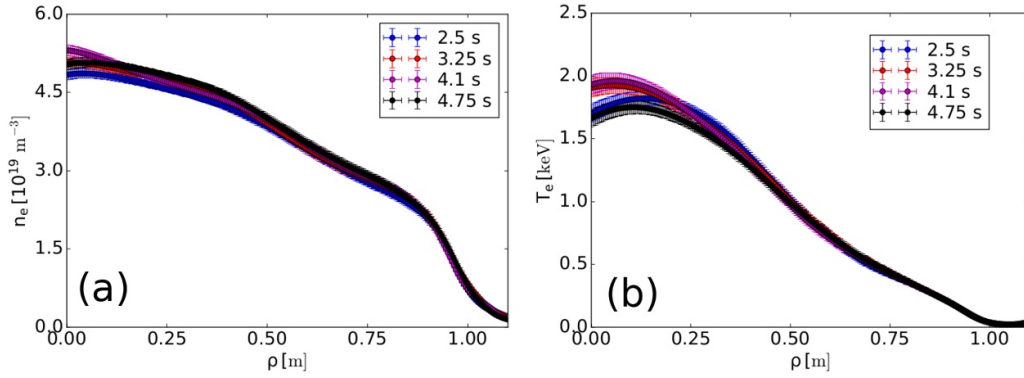


Figure 2. Radial profiles of electron (a) density and (b) temperature as a function of normalized toroidal flux ρ for different periods during the RMP amplitude scan (shot number 172146). The RMP produces no significant variation in radial profiles at the radial positions of interest.

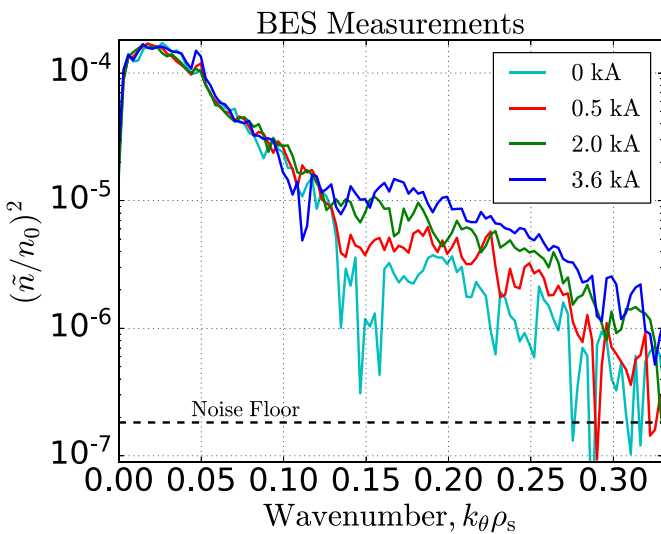


Figure 3. Experimental measurements of density fluctuation spectra taken with BES at $\psi = 0.88$, averaged in time over each phase of the I-coil current scan. There is an increase in density fluctuations with increasing RMP amplitude in the normalized poloidal wavenumber range $k_\theta \rho_s \approx .15 - .3$, spatial scales commonly associated with microturbulence. There is a 10% uncertainty in the calibration factor used to convert BES data to normalized density fluctuation. The horizontal dashed line represents the noise floor in the measurements.

with comparable growth rates. Eigenvalue calculations [33] are used to identify both modes simultaneously at each k_y . The ITG mode is localized to ion gyroradius scales, while the TEM continues to grow beyond $k_y \rho_s \approx 1$, likely transitioning into an electron-temperature-gradient (ETG) mode. Note that no numerical RMP was included in these simulations, and the RMP label refers solely to the unperturbed equilibrium at a given RMP point of the experimental scan.

The absolute radial profiles from experiment do not vary significantly with RMP amplitude, and the variation in normalized gradients listed in table 1 falls within error bars comparable to those expected for DIII-D L-mode discharges at this radial location, as cataloged in figure 8 of reference [34].

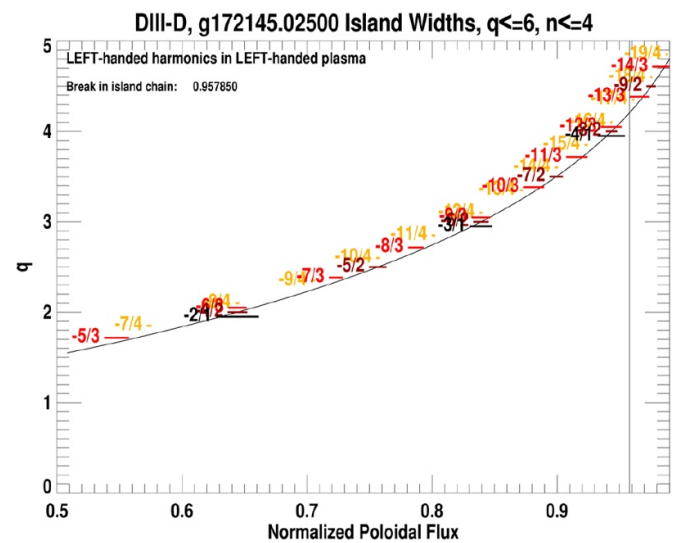


Figure 4. Profile of the safety factor q during the largest-RMP portion of the amplitude scan as a function of normalized poloidal flux. This work focuses on the variation of the $q = 10/3$ island (located at $\psi = 0.88$) with RMP amplitude. Plot generated using SURFMN [25].

However, as figure 5 shows, the discharge is located sufficiently close to the ITG-TEM transition that even such small changes can affect the dominant instability. While both ITG and TEM linear instabilities persist across all RMP amplitudes, the variations in growth rates suggest that the RMP has a nontrivial effect on equilibrium stability properties. It is, however, unlikely that the experimentally observed changes in density fluctuations with RMP amplitude can be attributed solely to changes in linear stability, as the growth rates vary non-monotonically with the RMP. This suggests that the key experimental observations can be attributed to non-linear physics.

3. Interaction of RMPs and Microturbulence

Nonlinear simulations are used to further explore what effect connects microturbulence and RMP amplitudes. These

Table 1. Physical parameters used for simulations performed at $\psi = 0.88$, the $q = 10/3$ flux surface. $\omega_X \equiv -(a/X)(dX/dr)$ represents normalized gradients, where $X = (n, T_{i0}, T_{e0})$ for equilibrium density, ion temperature, and electron temperature, respectively. The reference magnetic field $B_0 = 2.1$ T and the macroscopic reference length $a = 0.803$ m apply for all I-coil current values.

I-coil current	0 kA	0.5 kA	2.0 kA	3.6 kA
ω_n	2.903	2.198	2.396	3.142
$\omega_{T_{i0}}$	3.663	4.066	3.155	3.343
$\omega_{T_{e0}}$	5.708	5.016	5.958	5.797
\hat{s}	2.376	2.335	2.284	2.258
$\nu_c [10^{-2}]$	1.143	1.234	1.086	1.076
T_{i0} [keV]	0.393	0.370	0.385	0.406
T_{e0} [keV]	0.219	0.222	0.233	0.235
$n_0 [10^{19} \text{ m}^{-3}]$	2.32	2.39	2.32	2.20
$\rho^* [10^{-3}]$	1.29	1.27	1.31	1.29

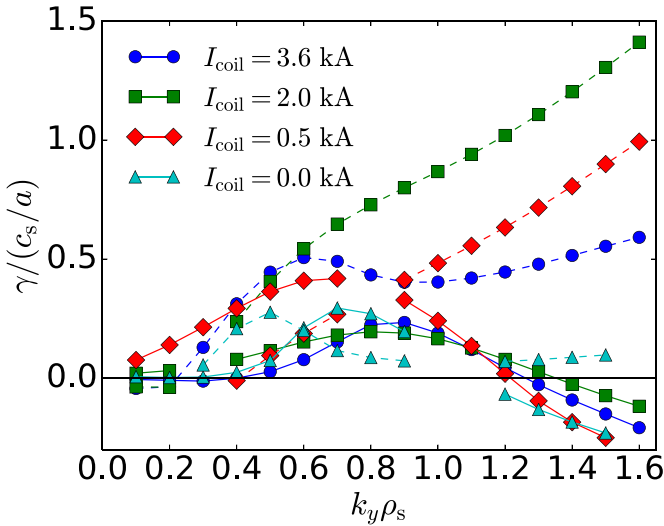


Figure 5. Variation in spectra of the linear growth rate γ with RMP amplitude at $\psi = 0.88$. Solid lines represent ion-direction modes (corresponding to ITG instability), dashed lines represent electron-direction modes (∇T -TEM). ITG instability is localized to $k_y \rho_s = 0.1 - 1$, while TEMs extend to higher k_y , eventually transitioning to ETG modes. c_s denotes the ion sound speed.

simulations include two kinetic species (electrons and deuterium ions) and resolve dynamics of both the large-scale RMP physics and the ion-scale microturbulence, with a minimum $k_y \rho_s = 0.015$ (corresponding to $n = 3$) and 128 $k_y \rho_s$ modes. For numerically converged fluxes, other resolution requirements are 192 k_x modes ($k_{x,\min} = 0.022$), 16 z , 32 v_{\parallel} , and 8 μ points.

The discussion that follows focuses on the $I_{\text{coil}} = 0.5$ kA equilibrium, which exhibits the least high- k_y ETG activity in non-linear simulations (despite not having the smallest growth rates at high- k_y) and consequently requires the fewest number of k_y modes among the four. Additionally, this equilibrium exhibits the strongest presence of ITG among the four linear instability spectra. As turbulence generated by the toroidal branch of ITG tends to be influenced significantly by zonal flow amplitudes, this equilibrium serves as the best candidate for examining the physics phenomenon of interest. To reiterate

an earlier statement, the other equilibria are within typical error bars for normalized gradients of the one selected here.

As previously mentioned, the magnetic geometry used for these calculations is generated from experimental data, but the magnetic structure does not include the RMP (even for the finite I-coil currents). Instead, magnetic fluctuations from the RMP are included as a constant-in-time, externally imposed magnetic potential of the functional form $A_{\parallel}^{\text{ext}} = A_{\parallel 0} e^{-z^2}$. For details of this implementation (including the definition of $A_{\parallel 0}$) and how it modifies the gyrokinetic Ampère's Law, see the appendix of reference [12]. The RMP is applied only at the radial $k_x \rho_s = 0$ and binormal wavenumber $k_y \rho_s = 0.015$, which corresponds to $n = 3$ and is an order of magnitude removed in spatial scale from the peak linear growth rate. The structure of the applied perturbation along the field line is tearing parity (a Gaussian $A_{\parallel}^{\text{ext}}$, *i.e.* an even function in z), which is crucial to observing the erosion of the zonal flow.

To establish a base scenario, a non-linear simulation without the applied RMP is run and allowed to reach a quasi-stationary turbulent state. The $A_{\parallel}^{\text{ext}}$ perturbation is then introduced, and the system is allowed to reach a new quasi-stationary state. This approach has been compared to simulations in which the perturbation was applied from the beginning. Both techniques result in the same saturated transport values, and the former is used in all results that follow. After application of the perturbation, B_r at the imposed k_y increases rapidly due to the plasma response until it saturates at the value of $k_y A_{\parallel}^{\text{ext}}$ (see figure 6). Values quoted for B_r/B_0 and ion electrostatic heat flux in the following discussion refer to those saturated amplitudes. It should be noted that there exists both electrostatic (associated with the $E \times B$ radial advection of particles) and electromagnetic (associated with the radial motion of particles streaming along perturbed field lines) transport present in these simulations. However, as the focus of this paper is on zonal flows (which regulate electrostatic transport), all transport quantities reported here are electrostatic.

The variation in electrostatic heat flux with radial magnetic field amplitude is shown in figure 7 for a range of B_r/B_0 amplitudes. Notably, the B_r values displayed are approximately an order of magnitude larger than those used in the experiment. This is a consequence of the β value of the simulations, which is artificially a factor of four lower than the experimental β , as discussed in the previous section. As the resultant quoted B_r amplitudes are a consequence of the externally imposed perturbation combined with the plasma electromagnetic response, a lower β means that the B_r produced by plasma magnetic response is correspondingly reduced and thus a larger imposed B_r is needed. More quantitatively, one needs to match the magnetic diffusivity [35, 36] resulting from both experiment and simulation. In computing the magnetic diffusivity D_{\parallel} from the non-linear simulation data, the analysis tool described in reference [15] was employed, with the average field line wandering calculated from a Poincaré plot of 200 radially-equidistantly seeded lines over 60 poloidal turns. The data for the experimental magnetic diffusivity is determined from the equilibrium vacuum field at each different point in the RMP amplitude scan, while the simulation magnetic diffusivity is determined from the saturated state, which includes

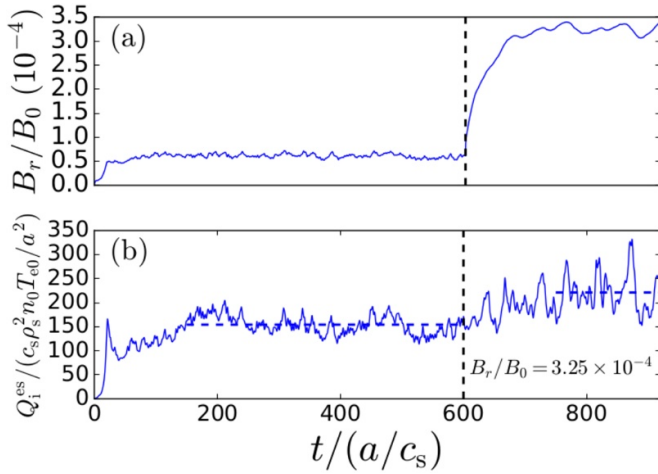


Figure 6. RMP impact on turbulent fluxes. In (a), upon switching on the RMP at time $t/(a/c_s) = 600$ (dashed black line), the amplitude of B_r/B_0 at the $k_{x,y}$ of the RMP grows until reaching the input RMP amplitude. Once this value is reached, a new quasi-stationary state is attained as evident in (b), in which the time-averaged ion heat flux (dashed horizontal line) saturates at a higher level with the RMP than without.

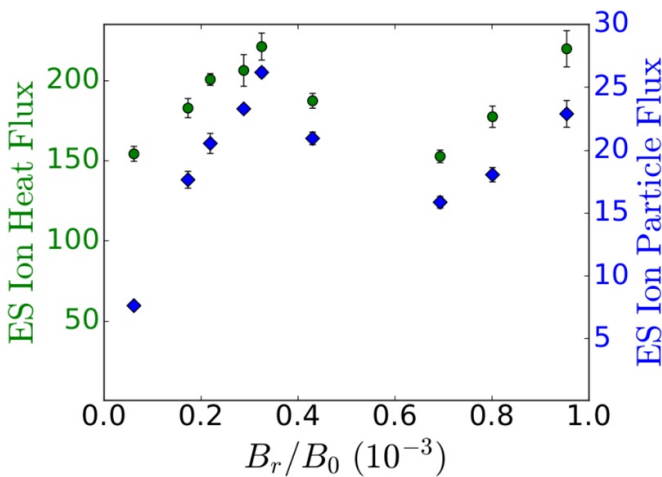


Figure 7. Electrostatic ion heat (green circles, normalized to $(c_s \rho_s^2 n_0 T_{e0}/a^2)$) and particle (blue diamonds, normalized to $(c_s \rho_s^2 n_0/a^2)$) flux versus radial magnetic field strength, showing non-monotonic behavior, which suggests the presence of physics beyond just zonal flow erosion. Error bars indicate standard deviations of time averaging the flux over the quasi-stationary state.

the plasma magnetic response. This difference means that the matching between experimental and computational quantities is not perfect, but still allows for a comparison of diffusivities, presented in figure 8. From the data shown there, one may conclude that B_r amplitudes required for the simulation are one order of magnitude larger than their experimental counterparts.

Returning to figure 7, the electrostatic transport scales non-monotonically with B_r . This applies to both the heat and particle transport channels; while this work focuses on heat fluxes, it is to be noted that the particle flux scaling matching that of the heat flux indicates no impact of the RMP on the

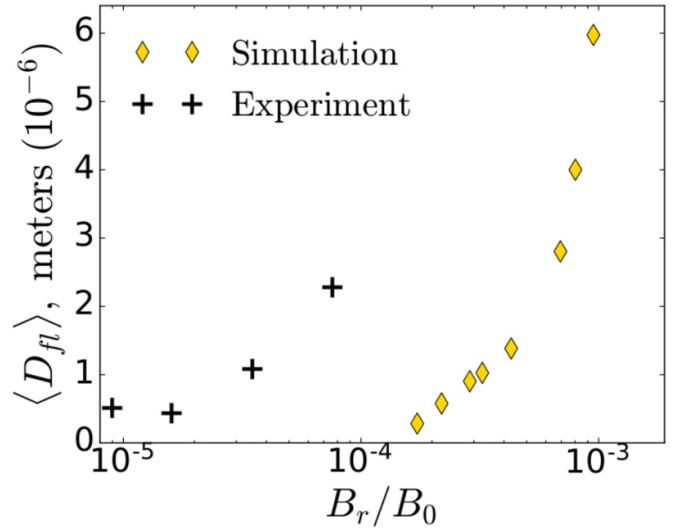


Figure 8. Magnetic field diffusivity versus radial magnetic field strength. The order-of-magnitude difference in B_r/B_0 between experiment and simulation needed to produce comparable magnetic diffusivity is attributed to the lower β used for simulation purposes. At the experimental β , the plasma accesses the regime for zonal-flow degrading magnetic flutter much more readily.

relevant transport-governing cross phases, and that the weak TEM flux argument mentioned in reference [37] does not apply here. Informed via the perspective of magnetic-flutter-induced zonal flow erosion, one may reasonably expect the electrostatic transport to increase monotonically with magnetic field perturbation. A mechanism for the observed drop in transport at intermediate B_r values arises from the effect of profile corrugations [38]. In flux-tube calculations, equilibrium pressure profiles are assumed flat and equilibrium pressure gradients constant. However, fluctuations in density or temperature perturbations vary over the radial domain when analyzed in time-average over a saturated state. These averaged perturbation profiles, referred to as corrugations, have their own gradients, which can serve as an additional turbulence drive on top of the equilibrium gradients [39, 40]. As seen in figure 9, which shows the radial profile of the perturbed ion temperature gradient $\tilde{\omega}_{T_i} \equiv -(a/T_i)(dT_i/dr)$, the corrugations are sinusoidal-like with a characteristic length scale—their corrugation length—of approximately $25 \rho_s$, while their amplitude is somewhat smaller than that of the equilibrium gradient.

If a large enough radial region is sampled by a particle moving along its trajectory, then the modifications introduced by these corrugations can average out. Generally, this occurs for radial excursions comparable to or larger than the corrugation length. When an RMP is applied at a resonant surface, an island forms, allowing particles to move very rapidly in the radial direction by one island width. As such, a comparison of corrugation length and island width illuminates the physical mechanism at play here. For the purposes of this discussion, an island width refers to maximal radial excursion of a given field

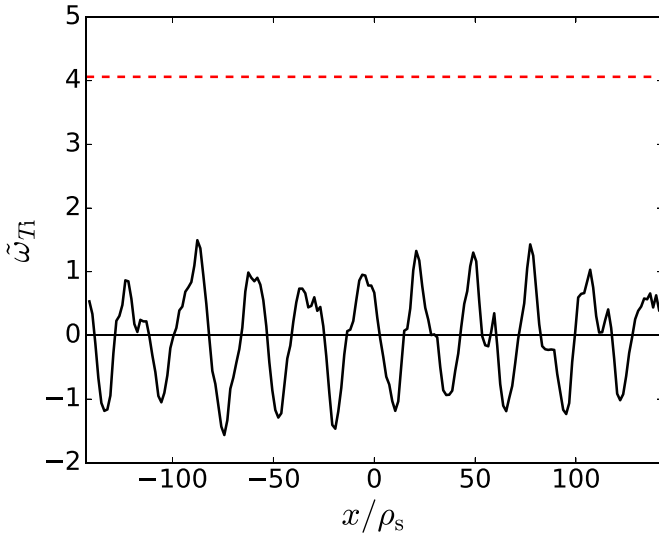


Figure 9. Temperature profile corrugations of a simulation with an external $B_r/B_0 = 3.25 \times 10^{-4}$, $\tilde{\omega}_{T_i} \equiv -(a/T_i)(dT_i/dr)$, where T_i is the fluctuating ion temperature. The black curve shows fluctuations in ion temperature gradient versus radial position, which exhibit periodic behavior and are localized in the x direction. The dashed red line corresponds to the equilibrium gradient ($\omega_{T_{i0}} \equiv -(a/T_{i0})(dT_{i0}/dr)$), which is constant, and fixed in these simulations via the flux-tube approximation. These corrugations are produced via time averaging turbulent fluctuations as depicted in figure 6 from 750 to 915 a/c_s .

line. This extends beyond the clean island-shaped flux surfaces, but more accurately corresponds to the physically relevant scale length which a streaming particle traverses radially. When this island width is less than half a corrugation length, particles moving rapidly within the island will only sample the radial region of enhanced gradient, and subsequently will feel an increased turbulent drive due to the corrugation. However, once the island width exceeds approximately half the corrugation length, the average corrugation effect experienced by a particle moving within the island begins to decrease as it samples regions of both increased and decreased gradients, until it vanishes entirely once the island width reaches a full corrugation length.

The non-monotonicity of the flux scaling with B_r can be matched to this phenomenon. Figure 10 shows island structures overlaid on contours of turbulent temperature fluctuations for the RMP values that correspond to the first peak (left) and the trough (right) in flux as shown in figure 7. Importantly, the corrugation length (here $\approx 25\rho_s$) can be seen not to vary with RMP amplitude, but rather to correspond to the scale length set by the lowest finite k_x that is coupled to the $k_x = 0$ mode through the parallel boundary condition [41]. This is in contrast to the island width, which is known to scale as $B_r^{1/2}$ (see e.g. reference [5]). The RMP island width corresponding to the first peak in transport is equal to approximately half the corrugation length, and thus the decrease in transport that comes with larger island widths is consistent with the physical picture described above. Additionally, the island width corresponding to the trough in transport matches well with the full corrugation length. Beyond this point, island self-overlap

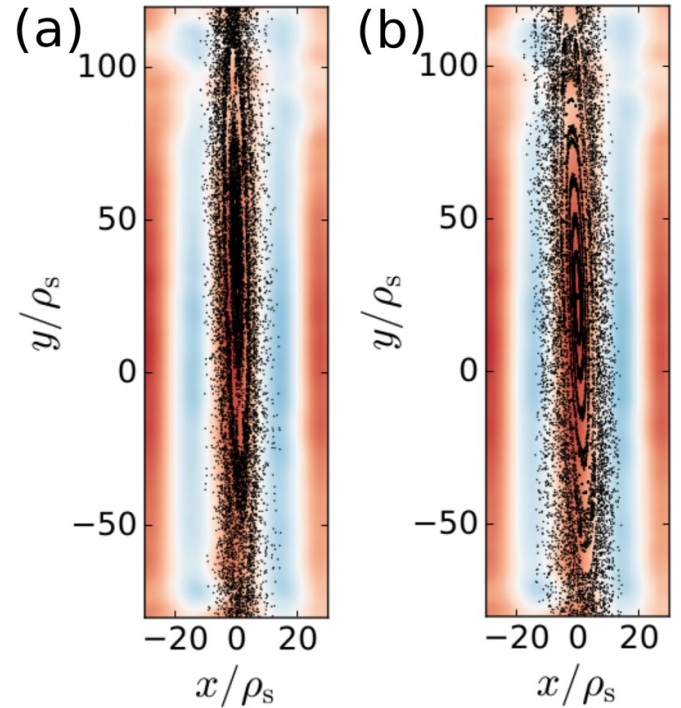


Figure 10. Poincaré plots of RMP island structure overlaid on contours of the time-averaged turbulent temperature gradient fluctuations for the RMP values corresponding to (a) the first peak in transport and (b) the trough, referring to figure 7. In (a) the RMP island width is approximately half a corrugation length, and particles traversing within the island experience only an increase in the driving gradient. In (b), the island width reaches a full corrugation length, and the increase and decrease in gradient experienced by particles moving within the island approximately cancel. Color scale ranges from 1 (red) to -1 (blue).

begins to occur, which greatly enhances the already present magnetic-flutter-induced zonal flow erosion, and which is now much stronger than the effect of corrugations. This corrugation effect is a consequence of using flux-tube simulations; for a more quantitative analysis at such higher RMP amplitudes, one would have to take the precise safety factor profile into account, relying on radially global simulations.

With a better understanding of these phenomena in hand, the effect of the RMP on microturbulence levels can now be more directly examined. Figure 11 plots density-fluctuation wavenumber spectra taken from simulations, focusing specifically on RMP strengths that result in magnetic diffusivity comparable to that seen in the experiment (see figure 8 for reference). In the experiment, even in the absence of an RMP, there still exists a small island at $\psi = 0.88$. As the existence of this island is suppressed by the artificially reduced β , the smallest imposed B_r/B_0 value in figure 11 serves as a proxy for this *no-RMP* island, and the curves in the figure can be compared to the curves of corresponding color in figure 3. Figure 11 shows the turbulence to increase with increasing RMP amplitude for a range of microinstability wavenumbers, agreeing well with the BES measurements of figure 3. Thus, simulations confirm the experimental finding that for increasing

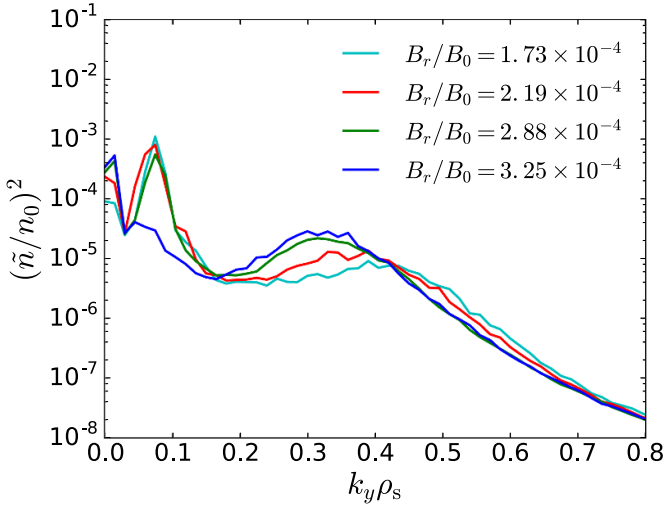


Figure 11. Density fluctuation amplitude vs. wavenumber. For the microinstability wavenumbers at which ITG dominates ($k_y \rho_s \sim 0.15 - 0.4$), the spectral amplitudes increase commensurately with RMP strength. This agrees well with the experimental results shown in figure 3, in which the microturbulence amplitude varied with RMP in the wavenumber range $k_\theta \rho_s \sim 0.15 - 0.3$.

RMP amplitudes—even at the low settings used in the experimental campaign—turbulence levels rise.

The density spectra exhibit interesting features outside of the microinstability wavenumber range for which fluctuations increase with RMP. Below $k_y = 0.1$, there are two peaks: one corresponding to the RMP applied at $k_y = 0.015$, and another peak at $k_y = 0.075$. The latter occurs at the largest scales for which ITG remains unstable (not shown in figure 5), and is reduced when the RMP is included. At the high- k_y end of the spectrum, where $k_y \gtrsim 0.5$, an increase in fluctuations with RMP is not observed. This can be attributed to a transition as seen in the linear instability spectrum from ITG to ∇T -TEM. It has been documented previously [42] that the impact of zonal flows on ∇T -TEM turbulence is very weak. As such, one would not expect the fluctuations at wavenumbers for which ∇T -TEM dominates to change in response to zonal flow reduction, in contrast to fluctuations at ITG-dominated wavenumbers (which depend strongly on zonal flows). It remains then to verify whether the changes observed for the ITG-dominated wavenumber range correspond to zonal flow erosion.

These simulations showing a range of microinstability fluctuations that vary with RMP amplitude, similar to the BES observations, suggest strongly that large-scale RMPs have a significant effect on small-scale microturbulence. However, it is important to study what specific aspects of the RMP govern this effect, and whether it can be directly connected to the previously discussed zonal-flow erosion mechanism or if the RMPs are increasing turbulence levels through a different process.

The $k_y = 0$ Fourier component of the electrostatic potential (*i.e.* the zonal mode amplitude) is plotted versus time in figure 12. After $t = 600 a/c_s$, when the RMP is applied, there

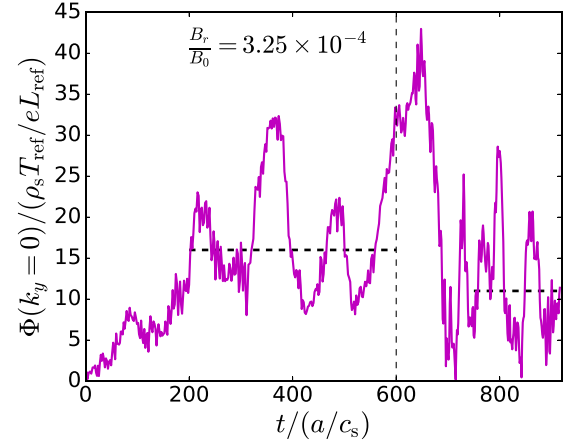


Figure 12. Time trace of the normalized $k_y = 0$ electrostatic potential Φ . After $t = 600$, the RMP is turned on, at which time the zonal flow amplitude drops and establishes saturated value 30% lower than before the RMP. This is evident from comparing the dashed black lines, which represent time averaged zonal flow amplitude before and after $t = 600$. The time window for averaging after RMP application is $t = [750 - 920] a/c_s$, set by the point at which the B_r perturbation saturates (see figure 6(a)) This decrease is consistent with the physical picture of zonal flow reduction via magnetic flutter.

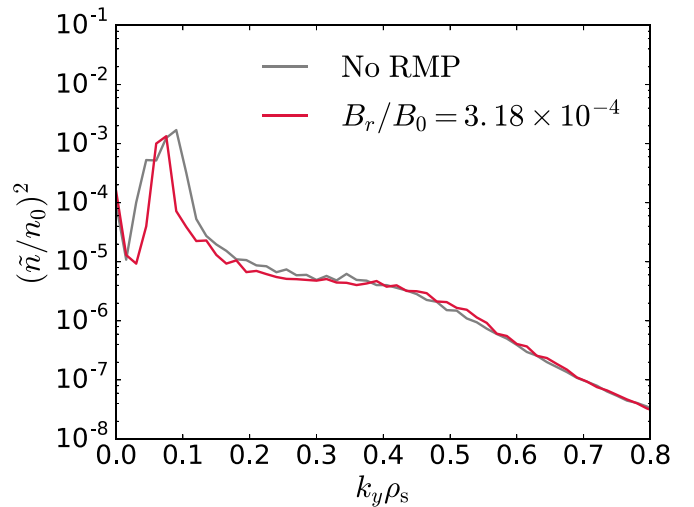


Figure 13. Density fluctuation amplitude vs. wavenumber, comparing spectra in a case without any applied RMP (gray) with a case that has an odd-parity, kink-like RMP (crimson) of comparable B_r amplitude to the tearing-parity studies. The addition of the odd-parity RMP does not produce a significant difference in the density fluctuation spectrum, in contrast to earlier results with the even-parity RMP.

is an observed drop in the zonal flow amplitude, occurring after an initial burst in zonal flow amplitude that is consistent with increased turbulence drive and a corresponding secondary instability [43] enhancement, before the erosion effect takes over again. Once the applied B_r perturbation saturates at its maximum value (around $t = 750 a/c_s$, as shown in figure 6), the zonal flow establishes a lower saturated value. Comparison of the time-average zonal flow amplitudes before and after the application of the B_r perturbation reveals a 30% decrease

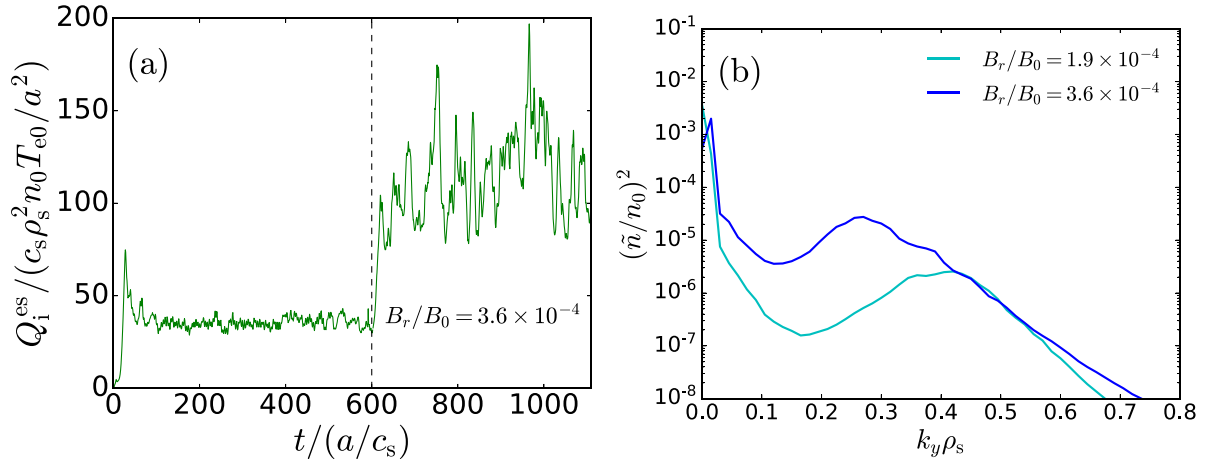


Figure 14. The effect of an RMP on turbulence in a modified maximum I-coil equilibrium, with gradients adjusted within error bars typical for DIII-D L-mode plasmas. Modification of ion and electron temperature gradients by 10% change the turbulence from ∇T -TEM-dominated to ITG-dominated. For the modified maximum I-coil equilibrium, both the (a) electrostatic ion heat flux and (b) density fluctuations increase with RMP, as was seen for the minimum I-coil equilibrium.

in amplitude. This indicates that these DIII-D L-mode discharges represent another regime in which multi-scale interaction between large-scale magnetics and zonal-flow-mediated microturbulence is significant, analogous to the previously discussed results of tearing modes and microturbulence in the reversed-field-pinch.

As briefly mentioned earlier, the z -structure of the imposed $A_{\parallel}^{\text{ext}}$ perturbation plays an important role in the zonal-flow erosion phenomenon. In this context, z refers to the field-line-following coordinate varying from $(-\pi, \pi]$, with $z=0$ denoting the outboard midplane. All of the preceding discussion has been based on a tearing-parity structure for the perturbation, where $A_{\parallel}^{\text{ext}} \propto e^{-z^2}$, which results in the breaking of flux surfaces. This contrasts to previous work on the interaction of RMPs and microturbulence on DIII-D [20], where the applied RMP had a kink-like—or ideal-MHD—structure that did not break flux surfaces. The kink-like RMP simply shifted flux surfaces without changing the magnetic topology. To examine how the results of that work fit into the physics discussion of this paper, the procedure detailed above for studying RMP effects was repeated but changing the RMP structure from even to odd parity in the field-line-following coordinate z . To reiterate, this parity definition is distinct from the RMP coil parity on the DIII-D experiment, and instead uses *even* for tearing-like perturbations and *odd* for ballooning-like perturbations that simply shift the surface. Figure 13 demonstrates the result of adding a perturbation of the form $A_{\parallel}^{\text{ext}} \propto ze^{-z^2}$ to a simulation: this odd-parity RMP has no appreciable effect on the density fluctuation spectra (aside from a slight narrowing of the low- k_y ITG peak), though the B_r magnitude is comparable to largest B_r value in figure 11. As the zonal flow follows flux surfaces, particles streaming along a perturbation that shifts flux surfaces rather than breaking them do not traverse regions of different electrostatic potential, so one does not expect the magnetic-flutter-induced shorting out of zonal flows to occur here. Not shown in the figure is the heat flux, which similarly does not undergo any significant change. This result demonstrates consistency between the physics

observed in the current work and reference [20], and highlights the necessity of breaking magnetic topology for zonal-flow erosion.

It should be noted that while the physics discussed in this section focused on the minimum I-coil amplitude equilibrium, similar results are possible for the other I-coil scenarios to within experimental uncertainties. Based on the parameters outlined in table 1, each of the other equilibria in the RMP amplitude scan are ∇T -TEM-dominated across all the microturbulent k_y , and as such the turbulence levels are not strongly dependent upon zonal flow amplitudes. When studying the effect of the RMP on these equilibria, a rise in turbulence and correspondence weakening of zonal flow activity is not observed. However, exemplarily increasing ω_{Ti} and decreasing ω_{Te} by 10% each for the maximum I-coil equilibrium leads to ITG-dominated physics over a range of wavenumbers analogous to the minimum I-coil equilibrium. Adding an RMP to this modified equilibrium produces the same result as discussed above, with the turbulence (both flux and density fluctuation amplitudes) increasing markedly with RMP amplitude (see figure 14). Note that for this case, the zonal flow amplitude—due to stronger turbulence drive—actually increases upon the addition of the RMP, but this effect is more than offset by the turbulence, resulting in larger fluxes.

4. Summary

A combined experimental and computational study of the inherently multi-scale effect of RMPs on zonal flows and microturbulence levels in an L-mode plasma in the DIII-D tokamak has been presented. This work is motivated by previous findings from gyrokinetic simulations of reversed-field pinches, which showed that magnetic fluctuations due to tearing modes play a significant role in setting microturbulence levels through zonal-flow erosion. Experimental measurements of density fluctuations using BES reveal a direct increase in fluctuation signal at microturbulent scales with

RMP amplitude, consistent with a similar interplay between magnetic fluctuations, zonal flows, and microturbulence. Turbulence simulations exhibit the same behavior over a range of RMP amplitudes, with a marked increase of turbulent fluctuations at the wavenumbers of linear ITG instability caused by the application of an RMP, with a corresponding drop in (either absolute or relative) zonal flow amplitude. This highlights the importance of taking turbulence into account when studying RMPs in the context of ELM suppression.

There are several aspects of RMP dynamics in tokamaks that are not addressed here. One concerns the role of plasma rotation. The plasma response to imposed islands generally results in island healing, which would reduce the size of an imposed RMP. The effectiveness of this response is reduced in the presence of bulk flows. It is known that some DIII-D plasmas are subject to significant equilibrium plasma flows (though less so in general in the L-mode), and thus an important question to examine is how these flows affect the RMP-zonal flow-microturbulence interaction discussed in this work. RMPs are also known to increase the L-H transition threshold. The physics involves pedestal fluctuations, flows, and a response to the RMP with rich physics, putting it outside the scope of the present work. Note, however, that the impact of flow on (partially) microstochasticized islands, such as the ones observed here, may differ from the idealized case.

There is still a wealth of physics to be explored involving this important multi-scale interaction between large scale magnetic fluctuations and microturbulence. As the physics discussed in this paper is centered around zonal-flow mediated turbulence, it would be worthwhile to examine the role that RMPs play in turbulence for which zonal flows are less significant. An experiment for which the plasma edge is more definitively in a ∇T -TEM regime, such as that discussed in reference [44], would provide an interesting contrast to the experimental discharges examined here.

While the numerical model of an externally imposed, constant-in-time large-scale magnetic fluctuation works well to describe RMPs, it does not accurately depict physical scenarios in which the large-scale magnetic fluctuations are driven from the plasma dynamics. Key examples in which significant large-scale magnetic activity arises naturally via plasma dynamics include the reversed-field pinch and astrophysical plasmas. Investigations of this multi-scale interaction in which not only magnetic fluctuations affect microturbulence but the reverse effect is also present will be an area of focus moving forward.

Acknowledgment

The authors thank DIII-D for experimental run time and resources provided through its Discovery Science initiative. SHN thanks M. Koepke for assistance and DOE Award DE-SC0018036 for financial support. This work was supported by the U.S. Department of Energy, Office of Science, Fusion Energy Sciences, under Award Nos. DE-FC02-04ER54698, DE-FG02-85ER-53212, DE-FG02-04ER-54742, and DE-FG02-08ER54999, as well as by the National

Science Foundation through XSEDE computing resources, allocation No. TG-PHY130027.

ORCID iDs

T. Nishizawa  <https://orcid.org/0000-0003-1804-2308>
 M.D. Nornberg  <https://orcid.org/0000-0003-1786-4190>
 D.M. Orlov  <https://orcid.org/0000-0002-2230-457X>
 S.H. Nogami  <https://orcid.org/0000-0001-5660-3669>

References

- [1] Holland C. and Diamond P.H. 2004 *Phys. Plasmas* **11** 1043
- [2] Maeyama S., Idomura Y., Watanabe T.-H., Nakata M., Yagi M., Miyato N., Ishizawa A. and Nunami M. 2015 *Phys. Rev. Lett.* **114** 255002
- [3] Howard N.T., Holland C., White A.E., Greenwald M. and Candy J. 2016 *Nucl. Fusion* **56** 014004
- [4] Ishizawa A. and Nakajima N. 2007 *Nucl. Fusion* **47** 15401551
- [5] Waltz R.E. and Waelbroeck F.L. 2012 *Phys. Plasmas* **19** 032508
- [6] Zarzoso D., Casson F.J., Hornsby W.A., Poli E. and Peeters A.G. 2015 *Phys. Plasmas* **22** 022127
- [7] Hornsby W.A., Migliano P., Buchholz R., Grosshauser S., Weikl A., Zarzoso D., Casson F.J., Poli E. and Peeters A.G. 2015 *Plasma Phys. Control. Fusion* **58** 104028
- [8] Bañón Navarro A., Bardóczi L., Carter T.A., Jenko F. and Rhodes T.L. 2017 *Plasma Phys. Control. Fusion* **59** 034004
- [9] Leconte M., Diamond P.H. and Xu Y. 2013 *Nucl. Fusion* **54** 013004
- [10] Thuecks D.J., Almagri A.F., Sarff J.S. and Terry P.W. 2017 *Phys. Plasmas* **24** 022309
- [11] Carmody D., Pueschel M.J., Anderson J.K. and Terry P.W. 2015 *Phys. Plasmas* **22** 012504
- [12] Williams Z.R., Pueschel M.J., Terry P.W. and Hauff T. 2017 *Phys. Plasmas* **24** 122309
- [13] Terry P.W., Pueschel M.J., Carmody D. and Nevins W.M. 2013 *Phys. Plasmas* **20** 112502
- [14] Pueschel M.J., Terry P.W., Jenko F., Hatch D.R., Nevins W.M., Görler T. and Told D. 2013 *Phys. Rev. Lett.* **110** 155005
- [15] Pueschel M.J., Hatch D.R., Görler T., Nevins W.M., Jenko F., Terry P.W. and Told D. 2013 *Phys. Plasmas* **20** 102301
- [16] Rosenbluth M.N. and Hinton F.L. 1998 *Phys. Rev. Lett.* **80** 724
- [17] Evans T.E. et al 2006 *Nat. Physics* **2** 419–23
- [18] McKee G.R. et al 2013 *Nucl. Fusion* **53** 113011
- [19] Monreal P., Sánchez E., Calvo I., Bustos A., Parra F.I., Mishchenko A., Köniecs A. and Kleiber R. 2017 *Plasma Phys. Control. Fusion* **59** 065005
- [20] Holod I., Lin Z., Taimourzadeh S., Nazikian R., Spong D. and Wingen A. 2017 *Nucl. Fusion* **57** 016005
- [21] McKee G.R., Fonck R.J., Shafer M.W., Uzun-Kaymak I.U. and Yan Z. 2010 *Rev. Sci. Instr.* **81** 10D741
- [22] Evans T.E. et al 2005 *Nucl. Fusion* **45** 595607
- [23] Fujisawa A. et al 2007 *Nucl. Fusion* **47** S718
- [24] Gupta D.K., Fonck R.J., McKee G.R., Schlossberg D.J. and Shafer M.W. 2006 *Phys. Rev. Lett.* **97** 125002
- [25] Schaffer M.J., Menard J.E., Aldan M.P., Bialek J.M., Evans T.E. and Moyer R.A. 2008 *Nucl. Fusion* **48** 024004
- [26] Jenko F., Dorland W., Kotschenreuther M. and Rogers B.N. 2000 *Phys. Plasmas* **7** 1904
- [27] For code details and access, see www.genecode.org
- [28] Meneghini O. and Lao L. 2013 *Plasma Fusion Res.* **8** 2403009
- [29] Logan N.C., Grierson B.A., Haskey S.R., Smith S.P., Meneghini O. and Eldon D. 2018 *Fusion. Sci. Technol.* **74** 125134

- [30] St John H., Taylor T.S., Lin-Liu Y.R. and Turnbull A.D. 1994 *Plasma Physics and Controlled Nuclear Fusion Research 1994* (Seville, Spain, 26 September - 1 October 1994) **3** 603–14
- [31] Pfeiffer W.W., Davidson R.H., Miller R.L. and Waltz R.E. 1980 ONETWO: A computer code for modeling plasma transport in tokamaks *General Atomics Report No. GA-A16178*
- [32] Xanthopoulos P., Cooper W.A., Jenko F., Turkin Y., Runov A. and Geiger J. 2009 *Phys. Plasmas* **16** 082303
- [33] Faber B.J., Pueschel M.J., Terry P.W., Hegna C.C. and Roman J.E. 2018 *J. Plasma Phys* **84** 905840503
- [34] Holland C. 2016 *Phys. Plasmas* **23** 060901
- [35] Rechester A.B. and Rosenbluth M.N. 1978 *Phys. Rev. Lett.* **40** 38
- [36] Nevins W.M., Wang E. and Candy J. 2011 *Phys. Rev. Lett.* **106** 065003
- [37] Hein T., Angioni C., Fable E. and Candy J. 2010 *Phys. Plasmas* **17** 102309
- [38] Waltz R.E., Austin M.E., Burrell K.H. and Candy J. 2006 *Phys. Plasmas* **13** 052301
- [39] Waltz R.E. 2010 *Phys. Plasmas* **17** 072501
- [40] Pueschel M.J., Görler T., Jenko F., Hatch D.R. and Cianciara A.J. 2013 *Phys. Plasmas* **20** 102308
- [41] Beer M.A., Cowley S.C. and Hammett G.W. 1995 *Phys. Plasmas* **2** 2687
- [42] Dannert T. and Jenko F. 2005 *Phys. Plasmas* **12** 072309
- [43] Srintzi D. and Jenko F. 2007 *Phys. Plasmas* **14** 042305
- [44] DeBoo J.C., *et al* 2012 *Phys. Plasma* **19** 082518